Ocean Engineering 123 (2016) 131–145

Contents lists available at ScienceDirect

Ocean Engineering

journal homepage: www.elsevier.com/locate/oceaneng

Full-scale unsteady RANS simulations of vertical ship motions in shallow water

Tahsin Tezdogan *, Atilla Incecik, Osman Turan

Department of Naval Architecture, Ocean and Marine Engineering, Henry Dyer Building, University of Strathclyde, 100 Montrose Street, Glasgow G4 0LZ, UK

ARTICLE INFO

Article history:
Received 16 May 2016
Received in revised form
27 June 2016
Accepted 28 June 2016
Available online 20 July 2016

Keywords:
Seakeeping
Computational fluid dynamics
RANS solver
Shallow water
Ship motions

ABSTRACT

The seakeeping behaviour of a vessel in shallow water differs significantly from its behaviour in deep water. In shallow water, a vessel's motion responses to incident waves will be affected by hydrodynamic effects caused by the presence of a finite depth. Given that a vessel will sail in shallow water at various times during its service life, such as when entering harbours, it is important to have an understanding of the influence of shallow water on ship motions. In this study, using a commercial unsteady Reynolds–Averaged Navier–Stokes solver, a numerical study of ship motions in shallow water was carried out. Firstly, the characteristics of shallow water waves were investigated by conducting a series of simulations. Then, a full-scale large tanker model was used as a case study to predict its heave and pitch responses to head waves at various water depths, covering a range of wave frequencies at zero speed. The motion results obtained were validated against related experimental studies available in the literature, and were also compared to those from 3-D potential theory. The results were found to be in good agreement with the experimental data. Finally, it was shown that vertical motions were significantly affected by shallow water.

1. Introduction

Over the last decade, an increasing number of large ships, such as Very Large Crude Carriers (VLCC) have called for a need to understand the performance and behaviour of such ships in shallow water. As indicated by Oortmerssen (Oortmerssen, 1976), the draft of fully loaded VLCCs is so large that it is often necessary to dredge approach channels around harbours, to enable such ships to enter harbours without grounding. In addition to harbours, even some open sea areas (for instance some areas in the North Sea) can be regarded as shallow water.

These large vessels are loaded and unloaded in exposed areas, where they are moored or secured to buoys or jetties. These designated terminals are located as close to shore as possible, mostly in shallow water. In order to diminish the risk of grounding for these ships, and to design and construct channels appropriately, it is critical to study vertical ship motions (heave and pitch) in shallow water (Oortmerssen, 1976).

According to Oortmerssen (1976), limited water depth has a perceptible influence on ship motions in waves, in particular when the ratio of water depth to draft of the ship is less than four. He claims that this effect becomes significant when the water depth is less than twice that of the draft. Beukelman and Gerritsma (1982) later contested this claim, instead suggesting the ratio to be two and a half.

Ship motions in response to incident waves in shallow water are affected in two ways (Oortmerssen, 1976):

i. Firstly, the incoming waves are affected due to the presence of a finite water depth. The consequential wave forces/moments exerted on the vessel therefore vary from those in deep water conditions.
ii. Secondly, the hydrodynamic coefficients (added mass and damping) of the ship will change, stemming from the effect of the sea bed.

There have been many attempts to predict wave excited forces and moments on a vessel, and motion responses of a vessel, in shallow water. From a seakeeping perspective, the use of two-dimensional strip theory methods to predict ship responses to waves, using a deep water assumption, can give satisfactory results at moderate speeds for conventional ship geometries. However, the use of strip theory is questionable when applied to shallow water conditions, since viscosity effects are amplified when the keel is very close to the seabed (Beukelman and Gerritsma, 1982). Because the strip theory is a two-dimensional theory, it assumes that the water flow propagates entirely underneath the ship. However Oortmerssen (1976) claims that in shallow water, three-

* Corresponding author.
E-mail address: tahsin.tezdogan@strath.ac.uk (T. Tezdogan).

http://dx.doi.org/10.1016/j.oceaneng.2016.06.047

dimensional effects become considerably important because the water flow passes partly underneath the vessel and partly around the two ship ends. Even in some extreme cases, water can flow only around the ends of the vessel. This therefore causes a deviation from the two-dimensional flow features around the bow and stern ends.

Kim (1968) used strip theory in ship motion calculations for a finite water depth. His calculations assumed that the incident wavelength was comparable with the beam and draft of the ship. His approach provided reasonable results for vertical motions, whereas it did not give good results for lateral motions, specifically at lower frequencies.

Over the last five decades, potential flow theory-based three-dimensional methods have been used extensively to calculate the hydrodynamic responses of marine structures in both deep and shallow waters. There has therefore been a huge amount of research and opinion published in this specific area. As clearly summarised by Yuan et al. (2014), the research devoted to this specific area can be classified into two categories depending on the Green function adopted in the boundary integral formulation.

As explained by Yuan et al. (2014), in the first category, the translating and pulsating sources are distributed over the mean wetted body surface. In this approach, a Green function is adapted to satisfy the free surface and the radiation conditions. This can be regarded as an effective method for the zero speed problems; however it has some restrictions when the forward speed effect is taken into account. The reason for this can be explained by the fact that it cannot take into account the near-field flow condition, and the interaction between the steady and unsteady flow. A list of some of the studies in which this method was used is presented below.

Daubert (1970), Garisson and Chow (1972), Oortmerssen (1972), Boreel (1974), and Troesch and Beck (1974) are the pioneers who applied the 3-D techniques. They fall into the first category, for the calculation of wave loads on large offshore structures in a finite water depth. Following this, Oortmerssen (1976, 1976) successfully applied this numerical method to a tanker to calculate its wave excited forces, added mass and damping coefficients and motions when the vessel is stationary. He then compared his numerical results to the experimental data. In general, the level of agreement was found to be acceptable, except for the surge force and pitch and yaw moments in beam waves, which the author believed stemmed from asymmetry in the hull's shape. Later, Endo (1987) studied the motions of three-dimensional bodies floating freely in waves in shallow water. He calculated the hydrodynamic forces and wave loads of a rigid body using the surface source distribution method, with the same assumptions made as from linear wave potential flow theory. Li (2001) concluded that Endo's method provides more accurate seakeeping predictions in shallow water. Nonetheless, he suggested that some sections of Endo's code need to be altered. Then, Chan (1990) developed a three-dimensional numerical technique for predicting first and second order hydrodynamic forces on a vessel travelling in waves. He applied his code to a fully submerged ellipsoid, a half-submerged ellipsoid, a Series-60 ship and a 200 kDWT tanker, to predict their hydrodynamic properties. The obtained numerical results were found to be in good agreement with the available experimental data, except for roll and pitch damping coefficients and responses. The author hypothesises that the poor results in pitch and roll motions come from nonlinear effects in large roll amplitudes, and viscosity effects, which were ignored in his approach. By using this technique he also provided a discussion about the effect of heading, forward speed and water depth on the hydrodynamic forces and ship motions in his study.

The second category is termed the Rankine source panel method, which utilises a very simple Green function in its boundary integral formulation. The distinct difference of this method is that the singularities are distributed not only over the hull surface, but over the free surface and control surface, as well. In the Rankine source panel method, the body surface and the whole domain are described with an acceptable degree of fidelity and a large number of discrete panels. This method offers the advantage of being applicable to any ship geometry or floating body, and it can also model an arbitrary sea bed topology. In addition, this method enables the inclusion of nonlinearities in the free surface and the coupled behaviour between steady and unsteady wave potentials. The Rankine source panel method was first proposed by Hess and Smith (1964). Then, Sclavounos and Nakos (1988) developed a numerical method to model the propagation of water waves on a panelised free surface. Their approach showed that the Rankine panel method can be used to predict wave patterns and excitation forces. Their study caused the development of the formulation of ship motions in the frequency-domain, which enables fast computations. For example, Yuan et al. (2014) developed a three-dimensional Rankine panel method in the frequency domain to predict the hydrodynamic properties of ships advancing at very low forward speeds. They adopted the radiation condition of Das and Cheung (2012) in their code. As a case study, they used a 'Wigley III' hull travelling at different forward speeds. By comparing their results with the available experimental data, they concluded that the new radiation condition gives good solutions of the scattered wave patterns, and the obtained wave exciting forces and motion responses are compatible with the results from the related towing tank tests.

However, the linear methods cannot model any coupling with nonlinear external mechanisms. Therefore, Kring (1994) extended the use of the Rankine panel method to the time domain. This makes it possible to directly include any kind of external forces and nonlinear waves in the calculations. Kim and Kim (2013), for example, studied the motions of an LNG carrier in various bathymetries, using a Rankine panel method and by solving the nonlinear Boussinesq equations. They obtained the motion responses and the hydrodynamic coefficients of the vessel in shallow water in the time domain and compared their results to those in deep water conditions. Their findings showed that the hydrodynamic properties of the vessel are altered significantly as water depth decreases, particularly at lower frequencies. They also found that the nonlinear effects become more important as vessels enter shallow water, especially when they are exposed to waves of longer wavelengths. The only shortcoming in their study was that they did not validate their theory with any experimental results, hence one cannot assess how close their results were to the experiments, and under which circumstances their theory gives successful results.

The vast majority of the numerical research in this field relies on the assumptions from potential flow theory, including free surface effects. However, effects which are ignored in potential theory, such as breaking waves, turbulence and viscosity, are the most significant for shallow water problems and should therefore be included in the numerical codes. Reynolds–Averaged Navier–Stokes (RANS) approaches, for example, are very good alternatives to potential flow theory as they can directly account for viscous effects in their calculations.

Continued technological advances offer ever-increasing computational power, which can be utilised for viscous flow simulations to solve RANS equations in the time domain. As such, Computational Fluid Dynamics (CFD)-based RANS methods are rapidly gaining popularity for seakeeping applications. These methods have the distinct advantage of allowing designers to assess the seakeeping performance of a proposed ship during its design stages, thus enabling any necessary corrective action to be taken on the ship's design, before the vessel is actually built (Tezdogan et al., 2015).

In 1994, a CFD workshop was organised in Tokyo to discuss the implementation of steady RANS methods to provide a solution for free-surface flows around surface ships. As explained by Wilson et al. (1998), from that point onwards, RANS methods have been widely used in many marine hydrodynamics applications.

Later, in 2010, a workshop on numerical hydrodynamics was held in Gothenburg, which aimed to discuss the implementation of CFD in the field of ship hydrodynamics. Many institutions and organisations around the world contributed to the Gothenburg 2010 Workshop, with studies performed using three well-known ship hulls (the KVLCC2, the KCS, and the DTMB 5415) as benchmarks. The studies presented in the workshop gauged the numerical efficiency of CFD methods for the prediction of ship hydrodynamic quantities via comparison with the related experimental data (Larsson and Stern, 2011). For a detailed literature review on CFD applications in ship resistance and motion simulations in deep water, reference may be made to two recently published articles: Tezdogan et al. (2015) and Simonsen et al. (2013).

Recently, CFD-based RANS simulations have also been used to study shallow water problems, such as finite-bottom effects on ship resistance, ship squat, free surface wave patterns, ship-to-ship interactions and ship manoeuvrability.

Sakamoto et al. (2007) presented RANS simulations and validation studies for a high-speed Wigley hull in deep and shallow water utilising CFDShip-Iowa, a general purpose ship hydrodynamics CFD code. Their results include resistance predictions and wave pattern analyses for a range of forward speeds in calm waters. Following this, Jachowski (2008) carried out a study on the assessment of ship squat in shallow water employing Fluent, a commercial RANS solver. He used a model scale KCS to calculate its squat for several water depths at different ship speeds. Then, Zou and Larsson (2013), using a steady-state RANS solver (SHIPFLOW), performed a numerical study on the ship-to-ship interaction during a lightening operation in shallow water. They used an Aframax tanker and the KVLCC2 in model scale, both appended with rudder and propeller. Also, Prakash and Chandra (2013) studied the effect of confined waters on ship resistance at various speeds, using Fluent as a RANS solver. They concluded that the CFD technique can successfully be used to predict ship resistance and the free surface wave pattern in shallow water. Finally, Castiglione et al. (2014) investigated the interference effects of wave systems on a catamaran in shallow water. They used CFDShip-Iowa as a RANS solver to calculate the resistance and the interference factor of the DELFT catamaran in two separation distances at various water depths. Their simulations were carried out in calm water conditions.

During this literature review, it was noted that the majority of the numerical results obtained in shallow water were not actually validated. Although there are several benchmark data sets for researchers to compare their deep water results with, unfortunately no benchmark ship data exists for researchers studying shallow water problems. This shortfall was highlighted in the latest (27th) International Towing Tank Conference (ITTC) and it was concluded that knowledge of the motions of large ships and floating structures in shallow water still remains a challenging issue. The ITTC's Ocean Engineering Committee has therefore suggested the introduction of benchmark data, to validate numerical methods based on the potential theory or CFD (International Towing Tank Conference (ITTC), 2014).

In addition, to the best of our knowledge, no specific study exists which aims to predict the motion responses of a vessel to waves in shallow water, using a CFD-based RANS approach. Therefore, this paper addresses the gap in our current knowledge by calculating the vertical motions of a ship against head seas in shallow water, utilising a RANS solver. In this research, an unsteady Reynolds–Averaged Navier Stokes (URANS) approach was applied using the commercial CFD software Star-CCM+ version 9.0.2, which was developed by CD-Adapco. Additionally, the supercomputer facilities at the University of Strathclyde were utilised to allow much faster and more complex simulations.

Firstly, before starting the real ship motion simulations, the effect of a finite water depth on incoming waves was investigated by conducting a series of simulations in the absence of a ship model. In this part of the study, the intention was to observe the degeneration in the incident wave form due to the sea bottom effect. To do this, nonlinear waves were simulated in three different water depths, and the free surface elevation was measured at various locations within the solution domain.

Then, a 200 kDWT tanker was chosen for this study due to the availability of its geometry and experimental data conducted in shallow water, to validate our CFD model.

A full-scale tanker model was used for all simulations, to avoid scaling effects. The model was used without any appendages to mimic the real experimental conditions. All CFD simulations were performed in waves at a zero ship speed. The simulations were carried out in three different ratios of water depth to draft ($\delta=1.2$, 3.0 and 4.365). The obtained results for $\delta=1.2$ and 4.365 were compared to those taken from the experimental study of Oortmerssen (1976, 1976) and Pinkster (1980), respectively. During all of the simulations, the heave and pitch time histories of the vessel in question were recorded, free surface wave patterns were obtained and the free surface wave elevations in different locations alongside the ship model were monitored. The results will cover heave and pitch transfer functions (or Response Amplitude Operators, RAOs) of the vessel in question, covering a range of wave frequencies in various water depths.

This paper is organised as follows: Section 2 gives the main ship properties along with its lines plan, and introduces a list of simulation cases applied to the current CFD model. Then, in Section 3, the numerical setup of the CFD model is explained, with details provided in the contained sub sections. Following this, all of the results from this work, including validation and verification studies are shown and discussed in detail in Section 4. Finally, in Section 5, the main results drawn from this research are briefly summarised and suggestions are made for future research.

2. Ship geometry and conditions

The ship motion simulations in shallow water were applied to the full-scale 200 kDWT class large tanker. Taking precedence from the experiments conducted by Oortmerssen (1976, 1976) and Pinkster (1980), the rudder, propeller and bilge keels were not appended to the model. The main particulars of the ship are presented in Table 1, and its body plan is shown in Fig. 1 (Oortmerssen, 1976; Pinkster, 1980). A three-dimensional view of the vessel is illustrated in Fig. 2.

As waves approach a shore, they exhibit a reduction in wavelength (λ) and wave celerity (c), whilst the frequency remains the same. For a given wave period (T_w), the wavelength is predicted according to the dispersion expression, which relates wave period to wavelength, as given in Eq. (1), below.

$$T=\left[\frac{g}{2\pi\lambda}\tanh\left(\frac{2\pi h}{\lambda}\right)\right]^{-1/2} \quad (1)$$

where g denotes the gravitational acceleration ($g=9.81$ m/s^2) and h denotes water depth. Heave and pitch RAO curves will be plotted against the nondimensional frequency numbers, $\omega'=\omega\sqrt{L/g}$ (L: Length between the perpendiculars in metres, ω: wave frequency in rad/s).

Table 1
Main properties of the 200 kDWT tanker (Oortmerssen, 1976; Pinkster, 1980).

Length between perpendiculars (L_{BP})	310.00 m
Breadth (B)	47.17 m
Depth (D)	29.70 m
Loaded draft (T)	18.90 m
Displacement (Δ)	234,994 m^3
Block coefficient (C_B)	0.847
Midship section coefficient (C_M)	0.994
Prismatic coefficient (C_P)	0.855
Waterplane coefficient (C_{WP})	0.900
Ship wetted area (S)	22,804 m^2
Longitudinal centre of buoyancy (LCB) from the midship, fwd+	6.61 m
Vertical centre of gravity (KG) from the base line	13.32 m
Metacentric height (GM_t)	5.78 m
Transverse radius of gyration	17.00 m
Longitudinal radius of gyration	77.47 m

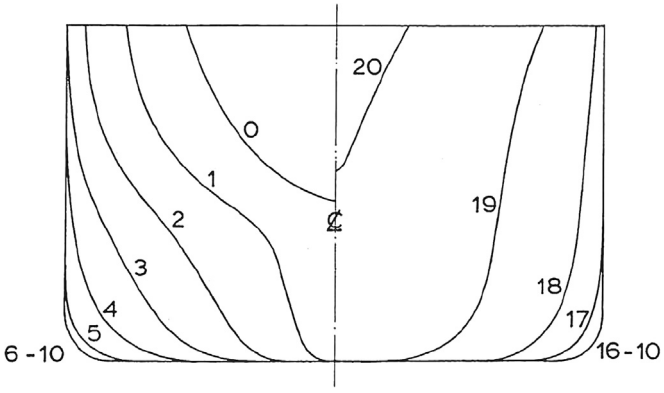

Fig. 1. Body plan of the tanker, taken from Oortmerssen (1976).

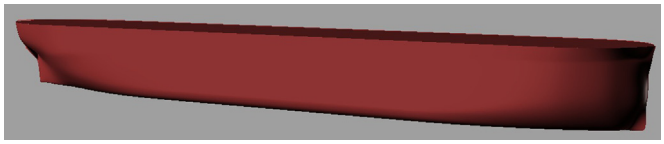

Fig. 2. A 3-D view of the tanker, modelled using Rhinoceros version 4.0.

The CFD simulations were performed at sixteen different conditions, as listed in Table 2, each identified by their case numbers. The characteristics of a wave are determined depending on the relationship between wavelength and water depth. It should be mentioned that in all the cases, the ratios of water depth to wavelength (h/λ) are below the value of 1/2, which corresponds to shallow water waves. The wavelength of each simulation case was calculated using Eq. (1). However, it should be borne in mind that Eq. (1) is based on linear wave theory, and therefore the resulting wavelengths in the simulations will be different from those listed in Table 2. Having said that, the waves considered in this work are not steep waves, and hence this deviation is not expected to have a significant effect on the results.

The nondimensional period number (τ) shown in the last column of Table 2 was calculated by $\tau = T_w(g/h)^{1/2}$. As will be discussed in Section 3.2, this number is helpful when deciding which wave model should be used to model regular head waves within the computational domain.

3. Numerical modelling set-up

Up until this point, this paper has provided a background to this study and has given an introduction to the work. The following section will provide details of the numerical simulation approaches used in this study and will discuss the numerical methods applied to the current CFD model.

3.1. Physics modelling

To model fluid flow, the solver employed uses a finite volume method, which uses the integral form of the conservation equations and divides the computational domain into a finite number of adjoining control volumes. In addition, the RANS solver employs a predictor-corrector approach to link the continuity and momentum equations.

The turbulence model chosen for use in this work was a standard k–ε model, which has been extensively used for industrial applications (International Towing Tank Conference (ITTC), 2014). Additionally, Querard et al. (2008) claim that the k–ε model is quite economical in terms of CPU time, compared to, for example, the SST turbulence model, which increases the required CPU time by nearly 25%. The k–ε turbulence model has also been used in many other studies performed in the same area, such as Kim and Lee (2011), Enger and Peric (2010) and Ozdemir et al. (2014). In addition to this, as reported in Larsson and Stern (2011), the majority of the numerical methods presented in the 2010 Gothenburg Workshop used either the k–ε or the k–ε turbulence model. At the workshop, most of the studies performed using Star-CCM+ as a

Table 2
Cases for which the CFD model is applied.

Case no. C	h/T δ	Wave frequency (rad/s) ω	Frequency number ω'	Wave-length (m) λ	Wave-length/L_{BP} λ/L_{BP}	Wave steepness H/λ	Period number τ	Wave speed (m/s) c
1.1	1.200	0.200	1.12	461.372	1.49	0.0118	20.66	14.69
1.2		0.300	1.69	301.539	0.97	0.0210	13.77	14.40
1.3		0.400	2.25	219.798	0.71	0.0222	10.33	13.99
1.4		0.500	2.81	163.301	0.53	0.0318	8.26	13.00
1.5		0.600	3.37	134.491	0.43	0.0333	6.89	12.84
2.1	3.000	0.200	1.12	712.292	2.30	0.0098	13.07	22.67
2.2		0.300	1.69	450.938	1.45	0.0140	8.71	21.53
2.3		0.400	2.25	313.347	1.01	0.0167	6.53	19.95
2.4		0.500	2.81	226.259	0.73	0.0199	5.23	18.01
2.5		0.600	3.37	166.535	0.54	0.0252	4.36	15.90
3.1	4.365	0.178	1.00	959.460	3.10	0.0071	12.17	27.18
3.2		0.267	1.50	602.305	1.94	0.0095	8.11	25.59
3.3		0.357	2.00	411.543	1.33	0.0139	6.07	23.38
3.4		0.443	2.50	295.753	0.95	0.0191	4.89	20.85
3.5		0.532	3.00	214.338	0.69	0.0188	4.07	18.15
3.6		0.623	3.50	158.342	1.49	0.0118	20.66	15.70

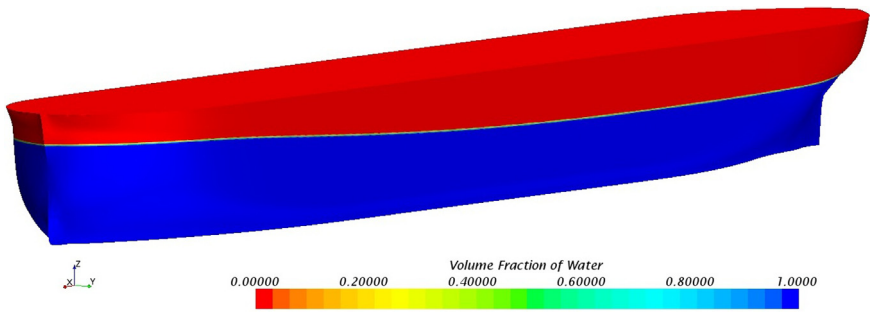

Fig. 3. Free surface representation.

RANS solver employed the standard k–ε model, as is used in this work. Lately, Tezdogan et al. (2015) performed URANS simulations using Star-CCM+, to predict heave and pitch motions, as well as the added resistance, of a full-scale KCS model in deep water conditions. They employed the k-ε model, and their results were found to be in good agreement with the available experimental results in the literature.

The "Volume of Fluid" (VOF) method was used to model and to position the free surface with a regular wave. In this study, a second-order convection scheme was used throughout all simulations in order to accurately capture sharp interfaces between the two phases, namely air and water. Fig. 3 demonstrates how the free surface was represented in this CFD model by displaying the water volume fraction profile on the hull. In the figure, for instance, a value of 0.5 for the volume fraction of water implies that a computational cell is filled with 50% water and 50% air. This value therefore indicates the position of the water-air interface, which corresponds to the free surface.

It should also be added that in the RANS solver, the segregated flow model, which solves the flow equation in an uncoupled manner, was applied throughout all simulations. Convection terms in the RANS formulae were discretised by applying a second-order upwind scheme. The overall solution procedure was obtained according to a SIMPLE-type algorithm.

In order to simulate realistic ship behaviour, a Dynamic Fluid Body Interaction (DFBI) module was used, with the vessel free to move in the pitch and heave directions. The DFBI module enabled the RANS solver to calculate the exciting forces and moments acting on the ship hull due to waves, and to solve the governing equations of rigid body motion in order to reposition the rigid body (Tezdogan et al., 2015; International Towing Tank Conference (ITTC), 2014).

3.2. Wave model

The commercial RANS solver employed in this study offers two suitable wave theories to describe regular waves: the fifth-order or the first-order Stokes waves. The theory of the fifth-order wave is based on the work of Fenton (1985). According to CD-Adapco (International Towing Tank Conference (ITTC), 2014), "this wave more closely resembles a real wave than one generated by the first-order method". However, Fenton (1985) points out that the fifth-order wave theory should not be used for large Ursell numbers (see Eq. (2)). Det Norske Veritas (DNV) (Det Norske, 2007) suggested that the fifth-order Stokes theory should only be applied to Ursell numbers less than 30. In addition, Fenton (1979) concluded in his study that for dimensionless period numbers greater than 8, the fifth-order Stokes wave theory should not be used, and that, instead, the fifth-order cnoidal wave theory should be used. Additionally, Fenton suggests the fifth-order Stokes waves should be used for nondimensional period numbers smaller than 8. Unfortunately, the RANS solver employed in this work does not provide the fifth-order 'cnoidal wave theory' to model incident waves and it is not possible to adjust the software package to model any other wave models. Given that linear wave theory can be used for all water depths, we used the first-order Stokes waves inside the solution domain for the cases with $\tau > 8$. For the other cases, the fifth-order Stokes waves were used to describe the wave at the inlet.

$$U_R = \frac{H\lambda^2}{h^3} \tag{2}$$

3.3. Choice of the time step

The Courant number is a useful indication to determine the time step. For time–accurate simulations, it should have an average value of 1 in all cells. This value signifies that the flow moves by about one cell size per time-step. If a second-order scheme is applied for time integration, in this case, the average Courant number should be less than 0.5.

Often, in implicit unsteady simulations, the time step is determined by the flow properties, rather than the Courant number. ITTC (International Towing Tank Conference (ITTC), 2014) recommends the use of at least 100 time steps per period for motion responses. In this study, a very small time step (1/256 of the wave period) was used over a simulation period. It is of note that a first-order temporal scheme was applied to discretise the unsteady term in the Navier–Stokes equations.

3.4. Solution domain and boundary conditions

An overset mesh, also known as Chimera or overlapping mesh, was used to facilitate the motions of the full-scale ship model due to the incident waves. Rigid and deforming mesh motion options are available in the software package, but these methods have distinct disadvantages compared to the overset mesh approach when simulating bodies with large amplitude motions. The rigid motion approach causes difficulties for free surface refinement, especially in pitch, and deforming meshes may lead to cell quality problems. On the other hand, the overset region, which encompasses the hull body, moves with the hull over a static background mesh of the whole domain (Field, 2013). For this reason, using the overset mesh feature of the software package saves computational costs, and allows the generation of a sufficiently refined mesh configuration around the free surface and the body, without compromising on the solution's accuracy.

When using the overset mesh feature, two different regions were created to simulate ship responses in waves, namely background and overset regions. A general view of the computational domain with the tanker hull model and the notations of selected boundary conditions are depicted in Fig. 4.

In order to reduce computational complexity and demand, only half of the hull (the starboard side) is represented. A symmetry

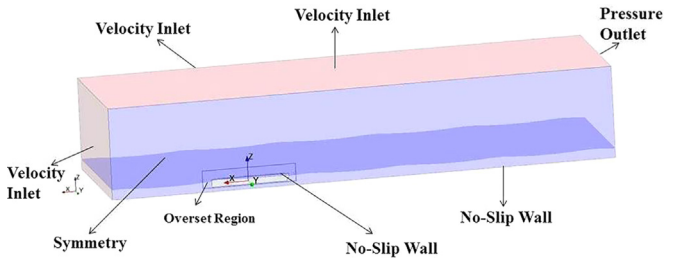

Fig. 4. A general view of the background and overset regions and the applied boundary conditions.

plane forms the centreline domain face in order to accurately simulate the other half of the model. It should be noted that in some figures given in this paper, the mirror image of the ship and domain is reflected on the port side for an improved visualisation.

Fig. 4 depicts that a velocity inlet boundary condition was set in the positive *x*-direction, where incident regular waves were generated. The initial flow velocity at this inlet condition was set to the corresponding velocity of the head waves. The negative *x*-direction was modelled as a pressure outlet since it fixes static pressure at the outlet. The top boundary was selected as a velocity inlet, whereas the bottom boundary was selected as no-slip wall boundary condition to account for the presence of the sea floor. The selection of the velocity inlet boundary condition for the top facilitates the representation of the infinite air condition. The symmetry plane, as the name suggests, has a symmetry condition, and the side of the domain (the negative *y*-direction) also has a velocity inlet boundary condition. These boundary conditions were used as they were reported to give the quickest flow solutions for similar simulations carried out utilising Star-CCM+ (CD-Adapco, 2014). The use of the velocity inlet boundary condition at the top and the side of the background prevents the fluid from sticking to the walls. In other words, it avoids a velocity gradient from occurring between the fluid and the wall, as in the use of a slip-wall boundary condition. Hence, the flow (including two phases: air and water) at the very top and very side of the background is directed parallel to the outlet boundary. This enables fluid reflections from the top and side of the domain to be prevented. It is of note that the top and side boundaries could have been set as a slip-wall or symmetry plane (Tezdogan et al., 2015).

Date and Turnock (1999) point out that, just as the selection of the boundaries is of great importance, their positioning is equally important. ITTC (International Towing Tank Conference (ITTC), 2014) recommends that, for simulations in the presence of incident waves, the inlet boundary should be located 1–2L_{BP} away from the hull, whereas the outlet should be positioned 3–5L_{BP} downstream to avoid any wave reflection from the boundary walls.

In this study, the size of the solution domain varied in each simulation case, depending on the wavelength of the incident waves. The locations of the boundaries used are illustrated in Fig. 5, which gives front and side views of the domain. As shown in the figure, we suggest that the inlet boundary should be positioned one wave length or one and a half ship lengths, (whichever is greater), away from the vessel, so that waves can be appropriately generated before encountering the vessel. Also, it should be highlighted that throughout all the cases, in order to prevent wave reflection from the walls, the VOF wave damping capability of the software package was applied to the background region with a damping length equal to at least one wavelength. This numerical beach model was used in downstream and transverse directions, as depicted in Fig. 5. For the wave damping modelling, Star-CCM+ adopts the method developed by Choi and Yoon (2009).

3.5. Coordinate systems

Two different coordinate systems were adopted to predict ship responses due to head seas in shallow water. The same procedure was applied by Simonsen et al. (2013) and Tezdogan et al. (2015) to monitor motions of a container ship in deep water. Firstly, the flow field was solved, and the excitation force and moments acting on the ship hull were calculated in the earth-fixed coordinate system. Following this, the forces and moments were converted to a body local coordinate system which was located at the centre of mass of the body, following the motions of the body whilst the simulation progressed. The equations of motions were solved to calculate the vessel's velocities. These velocities were then converted back to the earth-fixed coordinate system. These sets of information were then used to find the new location of the ship and grid system. The overset grid system was re-positioned after each time step.

3.6. Mesh generation

Mesh generation was performed using the automatic meshing facility in Star-CCM+, resulting in a computation mesh of circa 14 million cells in total. A trimmed cell mesher was employed to produce a high-quality grid for complex mesh generating problems. The ensuing mesh was formed primarily of unstructured hexahedral cells with trimmed cells adjacent to the surface.

The computation mesh had areas of progressively refined mesh size in the area immediately around the hull, as well as the expected free surface, to ensure that the complex flow features were appropriately captured. The refined mesh density in these zones was achieved using volumetric controls applied to these areas. Fig. 6 depicts a general view of the computational mesh showing the background and overset domains. Also, Fig. 7 provides a closer look at the volume mesh from above, around the ship geometry.

When generating the volume mesh, special attention was given to the overset region and the overlapping area. Firstly, it was ensured that the most refined mesh areas around the hull, such as the bow and stern, remained within the boundaries of the overset domain. In addition, it was ensured that the overlapping region consisted of at least 4 or 5 cell layers in both overset and background meshes. Also, it was verified that the cells in both meshes were of similar size on the overlapping region.

To simulate ship motions in waves, the free surface mesh was generated based on the guidelines for ship CFD applications from ITTC (International Towing Tank Conference (ITTC), 2014). According to these recommendations, a minimum of 80 cells per wavelength were used on the free surface. As proposed by Kim

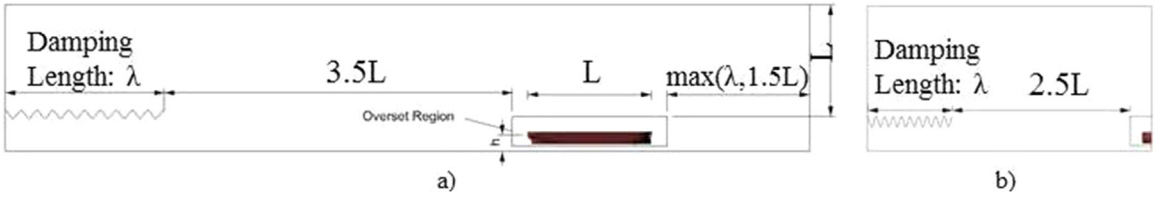

Fig. 5. The dimensions of the computational domain for the seakeeping simulations (a) front view, (b) side view.

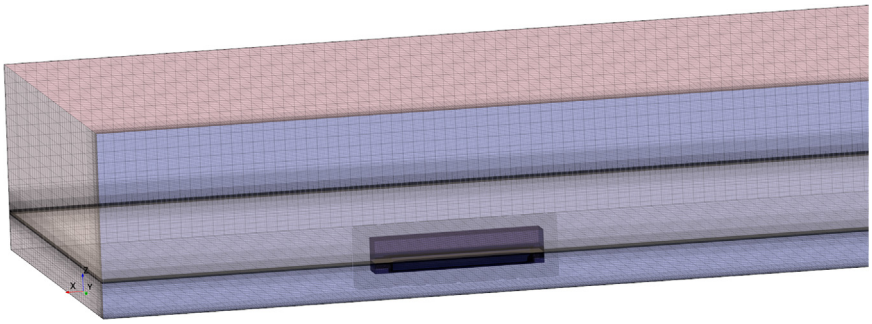

Fig. 6. A general 3-D view of the computational mesh.

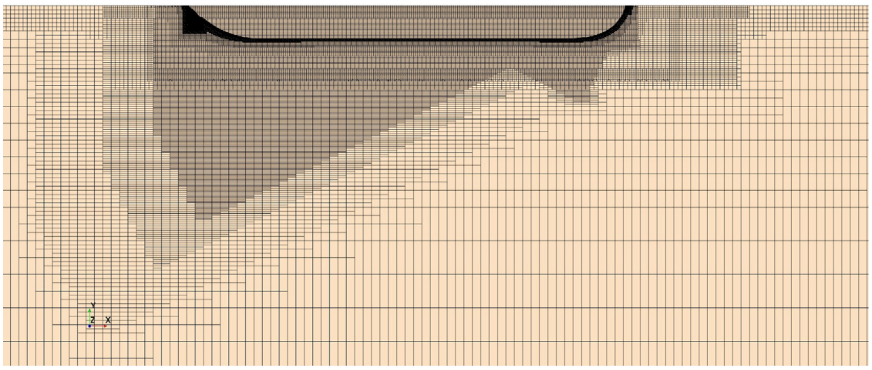

Fig. 7. A cross-section of the computation mesh from above, around the vessel geometry.

and Lee (2011), in order to capture the severe free surface flows such as slamming and green water incidents, a minimum of 150 grid points per wavelength were used near the hull free surface in both downstream and upstream directions. Additionally, a minimum of 20 cells were used in the vertical direction where the free surface was expected.

Fig. 8 shows the surface mesh on the ship hull. Fig. 9 displays the refined mesh area around the free surface regular waves. It should be noted that, for an improved visualisation, Fig. 9 is scaled by a factor of 10 in the vertical direction.

4. Results and discussion

This section, consisting of six sub-sections, will outline the simulation results obtained during this study, and will also provide some comparison with experimental results and the results from 3-D potential flow theory. It will then present a discussion on the results obtained.

4.1. Formulations

The transfer functions of heave and pitch motions were calculated as follows:

$$TF_3 = \frac{x_{31}}{\zeta_{I1}} \tag{3}$$

$$TF_5 = \frac{x_{51} L_{BP}}{\zeta_{I1}} \tag{4}$$

where x_{31}, x_{51} and ζ_{I1} are the first Fourier Series (FS) harmonic amplitudes of heave, pitch, and incident wave time histories, respectively. It must be clarified that in this study, the vertical motions were evaluated at the ship's centre of gravity.

4.2. Verification study

A verification study was undertaken to estimate the discretisation errors due to grid-size and time-step resolutions for Case 3.2 (h/T=4.365 and ω'=1.5). It is expected that the numerical uncertainties for the other cases are of the same order.

Xing and Stern (2010) state that the Richardson extrapolation (RE) method (Richardson, 1911) is the basis for existing quantitative numerical error/uncertainty estimates for time-step convergence and grid-spacing. With this method, the error is expanded in a power series, with integer powers of grid-spacing or time-step taken as a finite sum. Commonly, only the first term of the series will be retained, assuming that the solutions lie in the asymptotic range. This practice generates a so-called grid-triplet study. Roache (1998) grid convergence index (GCI) is useful for estimating uncertainties arising from grid-spacing and time-step errors. Roache's GCI is recommended for use by both the American Society of Mechanical Engineers (ASME) (Celik et al., 2008) and the American Institute of Aeronautics and Astronautics (AIAA) (Cosner et al., 2006).

For estimating iterative errors, the procedure derived by Roy and Blottner (2001) was used. The results obtained from these

Fig. 8. Surface mesh generated on the ship hull.

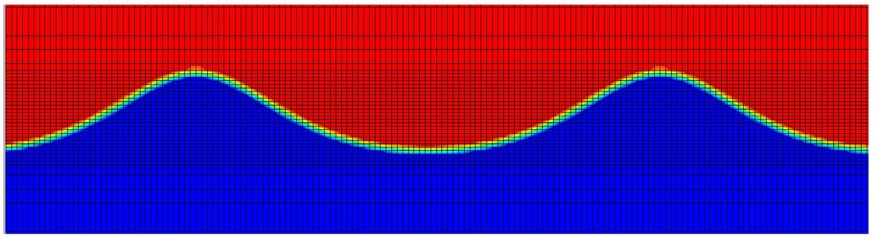

Fig. 9. A cross-section of the refined mesh area around the free surface waves (scaled by a factor of 10 in the vertical direction).

Table 3
The final cell numbers for each mesh configuration as a result of the applied refinement ratio to the overset mesh region.

Mesh Configuration	Cell Number (N)		
	Background	Overset	Total
Fine	5,474,918	10,255,979	15,730,897
Medium	5,474,918	6,976,206	12,451,124
Coarse	5,474,918	3,434,465	8,909,383

calculations suggest that the iterative errors for the heave and pitch transfer functions were 0.200% and 0.195% of the solution for the finest grid-spacing and smallest time-step, respectively.

Grid-spacing and time-step convergence studies were carried out following the grid convergence index (GCI) method described in Celik et al. (2008). The convergence studies were performed with triple solutions using systematically refined grid-spacing or time-steps.

To assess the convergence condition, the convergence ratio (R_k) is used, as given by:

$$R_k = \frac{\varepsilon_{k21}}{\varepsilon_{k32}} \tag{5}$$

where $\varepsilon_{k21}=\varphi_{k2}-\varphi_{k1}$ and $\varepsilon_{k32}=\varphi_{k3}-\varphi_{k2}$ are the differences between medium-fine and coarse-medium solutions, and φ_{k1}, φ_{k2} and φ_{k3} correspond to the solutions with fine, medium and coarse input parameters, respectively. The subscript k refers to the k^{th} input parameter (i.e. grid-size or time-step) (Stern et al., 2006).

Four typical convergence conditions may be seen: (i) monotonic convergence ($0<R_k<1$), (ii) oscillatory convergence ($R_k<0$; $|R_k|<1$), (iii) monotonic divergence ($R_k>1$), and (iv) oscillatory divergence ($R_k<0$; $|R_k|>1$). For diverging conditions (iii) and (iv), neither error nor uncertainty can be assessed (Stern et al., 2006). For convergence conditions, the generalised RE method is applied to predict the error and order-of-accuracy (p_k) for the selected kth input parameter. For a constant refinement ratio (r_k), p_k can be calculated by:

$$p_k = \frac{\ln(\varepsilon_{k32}/\varepsilon_{k21})}{\ln(r_k)} \tag{6}$$

The extrapolated values can be calculated from Celik et al. (2008):

$$\phi_{ext}^{21} = \left(r_k^p\phi_1 - \phi_2\right)/\left(r_k^p - 1\right) \tag{7}$$

The approximate relative error and extrapolated relative error can then be calculated using (Eqs. (8) and 9), respectively (Celik et al., 2008):

$$e_a^{21} = \left|\frac{\phi_1 - \phi_2}{\phi_1}\right| \tag{8}$$

Table 4
Grid convergence study for the heave and pitch TFs.

	TF_3 (*with monotonic convergence*)	TF_5 (*with monotonic convergence*)
r	$\sqrt{2}$	$\sqrt{2}$
φ_1	0.683	2.619
φ_2	0.694	2.636
φ_3	0.715	2.658
R	0.524	0.787
p	1.866	0.69
φ_{ext}^{21}	0.671	2.556
e_a^{21}	1.61%	0.649%
e_{ext}^{21}	1.80%	2.46%
GCI_{fine}^{21}	2.21%	3.00%

$$e_{ext}^{21} = \left|\frac{\phi_{ext}^{12} - \phi_1}{\phi_{ext}^{12}}\right| \tag{9}$$

Finally, the fine-grid convergence index is predicted by:

$$GCI_{fine}^{21} = \frac{1.25e_a^{21}}{r_k^p - 1} \tag{10}$$

It should be borne in mind that (Eqs. (6)–10) are valid for a constant r_k value. Reference can be made to Celik et al. (2008) for the formulae valid for a non-constant refinement ratio. The notation style of this reference was used in this study in order to enable the verification results to be presented clearly.

For both the mesh-spacing and time-step convergence studies, a constant refinement ratio (r_G) was chosen to be $\sqrt{2}$ in this study. It is of importance to mention that during the mesh convergence study, the refinement ratio was applied only to the overset region. This enabled the incident waves to be modelled efficiently through the computational domain. Without this adjustment, the wave would not have been captured well with a coarser grid configuration, causing misleading results. Based on this mesh refinement ratio, the final mesh numbers for each mesh configuration are listed in Table 3. Similarly, the time-step convergence study was conducted with triple solutions using systematically lessened time-steps, starting from $\Delta t=T_w/2^8$.

The verification parameters of the trim, sinkage and the total resistance coefficients for the grid spacing and time-step convergence studies are presented in Tables 4 and 5, respectively.

As can be seen from Tables 4 and 5, reasonably small levels of uncertainty were estimated for the obtained parameters. The numerical uncertainties in the finest-grid solution for TF_3 and TF_5 are predicted as 2.21% and 3.00%, respectively (Table 4). These values reduce to 1.48% and 1.78%, respectively, when calculating the numerical uncertainty in the smallest time-step solution (Table 5). It can be interpreted that the very small uncertainty results for the time-step convergence study are due to the selection of very small time-step resolutions in the simulations. Also, it is obvious that the pitch transfer function is more sensitive to the grid-spacing compared to the heave transfer function.

Table 5
Time-step convergence study for the heave and pitch TFs.

	TF_3 (*with monotonic convergence*)	TF_5 (*with monotonic convergence*)
r	$\sqrt{2}$	$\sqrt{2}$
φ_1	0.683	2.619
φ_2	0.692	2.634
φ_3	0.711	2.655
R	0.474	0.714
p	2.156	0.971
φ_{ext}^{21}	0.6749	2.5815
e_a^{21}	1.32%	0.57%
e_{ext}^{21}	1.20%	1.45%
GCI_{fine}^{21}	1.48%	1.79%

4.3. Wave generation

Understanding the behaviour of nonlinear shallow water waves is critical not only for coastal structures but for CFD standing points as well. From a CFD point of view, the area in the domain where the free surface is expected should be predicted, in order to mesh this area more finely. We therefore performed a series of simulations to observe the wave form throughout the solution domain, before starting the fundamental ship motion simulations in shallow water. To do this, the overset region, including the ship model, was omitted, leaving only the background domain, which is demonstrated in Fig. 4. In this specific study, the numerical damping was only applied in the downstream direction in the computational domain. It should also be mentioned that a second-order temporal scheme was applied in order to conduct this study on waves.

Troesch and Beck (1974) also performed such wave analyses experimentally before conducting seakeeping experiments with a ship model in shallow water, concluding that, "sinusoidal waves in shallow water are unstable and will degenerate fairly rapidly. In order to conduct the ship motion experiments, a knowledge of this process is essential". Also, many years ago, Korteweg and Vries (1895) theoretically investigated nonlinear shallow water problems. Their study particularly focused on the change of form of long waves advancing in a rectangular canal, by using a perturbation expansion on particle velocities, which has since borne their name in the literature.

Firstly, the degeneration of the shallow water waves as they advance inside the domain was investigated in a similar way to the experiments of Troesch and Beck (1974). For each three water depth conditions ($\delta=1.2$, 3.0 and 4.365), the first harmonic amplitudes of a fifth-order Stokes wave ($T_w=12.133$ s) as a function of distance down the inlet were calculated, aided by wave probes located at various distances from the inlet. The results obtained from this study's CFD work are demonstrated graphically in Fig. 10. In the figure, the harmonic amplitudes were divided by the calculated wave amplitude at the inlet (ζ_o), and the distances (X) were non-dimensionalised with respect to the actual wavelength (λ). It is worth-noting that the same wave is generated at the inlet in all three cases ($T_w=12.133$ s, $H=5.66$ m).

The results presented in Fig. 10 show that the first FS harmonic wave amplitudes mostly decrease as the wave travels through the domain. As can be observed from the figure, the variation in wave amplitudes is most pronounced at Wave 3 ($\delta=4.365$), followed by Wave 2 ($\delta=3.0$). This is because Wave 3 has the longest wavelength amongst the three studied waves. It should be borne in mind that the period number of Wave 1 ($\delta=1.2$) is 7.98, a value where the fifth-order wave theory is still applicable.

As discussed above, the 1st harmonic wave amplitudes varied along the simulation domain length. Therefore, for each simulation case, an average was taken of the wave amplitudes measured at three wave probes, located along the ship's length, to be used in the calculation of the transfer functions (see (Eqs. (3) and 4)).

Fig. 11 shows a comparison of the waves generated inside the domain (just after the symmetry plane) at different water depths. This figure also compares the appearances of the first- and fifth-order waves simulated at a water depth of 22.68 m. The simulations used to form Fig. 11 were run for 10 wave periods, and the snapshots seen in the figure were taken after the simulations completed their run. It should also be mentioned that these simulations were initialised using undisturbed free surface. In addition to this, Fig. 12 displays the free surface elevations at a distance of one wavelength away from the inlet, obtained using the first- and fifth-order Stokes wave theories. Wave 1 was used to provide the comparison shown in Fig. 12.

Figs. 11 and 12 jointly confirm that the resulting wave shape, obtained using the first-order wave theory, is different from the sinusoidal wave form. It is obvious that the obtained wave shape is degenerated as it propagates down the inlet. This result is in agreement with the experimental findings of Troesch and Beck (1974). From the comparison of the first- and fifth-order wave theories provided in Figs. 11 and 12 in the shallowest water, it can be concluded that the simulated waves obtained using the fifth-order theory give more successful results compared to those using the first-order wave theory. Therefore it can be interpreted from these figures that the first-order wave theory is inadequate to generate a stable boundary condition for regular waves. As mentioned in Section 3.2, the first-order Stokes waves were used inside the solution domain for the cases with $\tau>8$. It is therefore expected that these cases have degenerating waves, as can be seen in Fig. 11(d).

It should be mentioned that, in order to obtain transfer function accurately, the wave steepness can be chosen as desired. Linear wave theory inlet boundary conditions can be used for this reason without producing degenerating waves provided that the wave steepness is very small. For steeper waves, higher order shallow water theories should be used as boundary conditions, to avoid wave degeneration and provide to obtain realistic ship forces/moments.

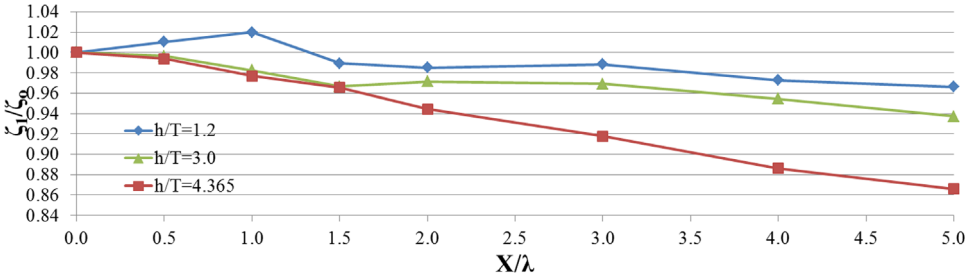

Fig. 10. Nondimensional 1st FS harmonic amplitudes plotted against nondimensional distance from the inlet at various water depth conditions ($T_w=12.133$ s).

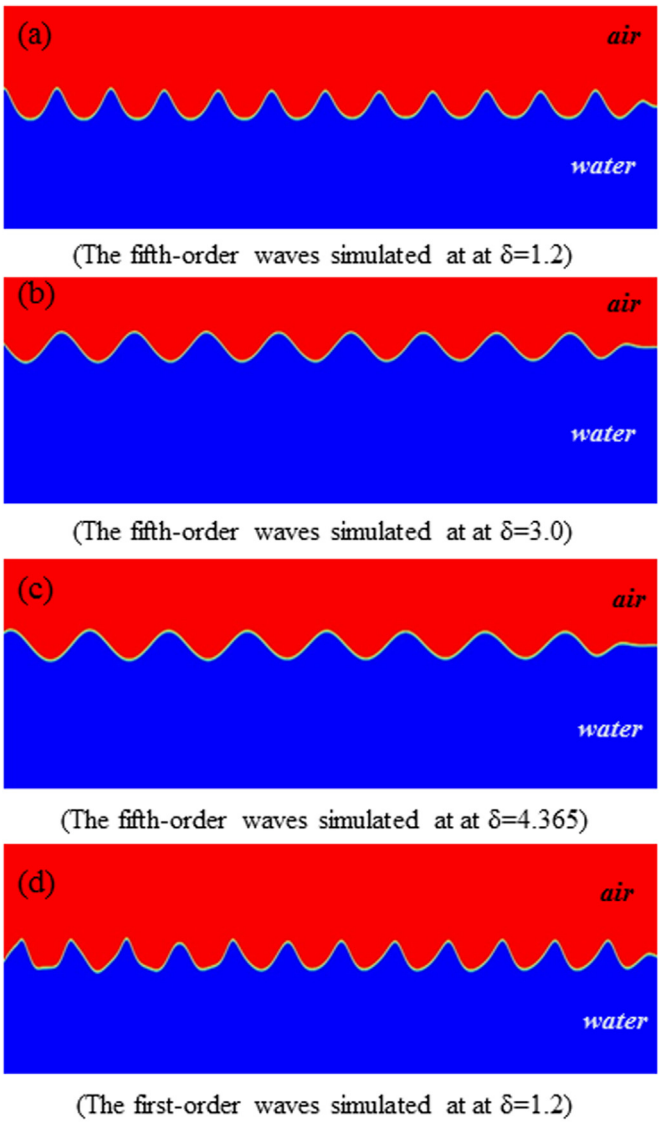

Fig. 11. A front view of the cross-sections of the simulation domain (just after the symmetry plane) with the waves (T_w=12.133 s, H=5.66 m) generated inside the domain (scaled by a factor of 20 in the vertical direction).

4.4. Wave contours

In this sub-section, wave contours generated by the presence of the ship model freely heaving and pitching around a free surface will be presented. Fig. 13 illustrates the wave patterns around the tanker in question generated by unit wave amplitude at a water depth of 22.68 m, for various non-dimensional frequencies (ω'=1.12, 1.69 and 2.25). As can be seen from the figure, as the waves become shorter, (in other words as the celerity of waves decrease), the wave contours become densely massed.

4.5. Transfer functions

The heave and pitch transfer functions obtained by the current CFD model were first validated against the experimental work of Oortmerssen (1976, 1976) and Pinkster (1980), and were also compared to those obtained using a potential flow panel method for the two water depth conditions, namely δ=1.2 and 4.365, respectively. The panel methods used in this comparison were developed by the same researchers, who used a 3-D Green function to satisfy free surface and radiation conditions in the frequency domain. The results from the potential flow panel method were adapted from the published studies of the abovementioned researchers. For more details on these numerical methods, reference may be made to Oortmerssen (1976, 1976), and Pinkster (1980).

For the two water depth conditions, the heave and pitch transfer functions obtained by all three methods are graphically compared in Figs. 14 and 15, below.

As can be seen from Figs. 14 and 15, the transfer functions, obtained using our URANS approach, are in fairly good agreement with the related experimental results. The discrepancies between our numerical results and the experimental results are more pronounced at δ=1.2, which corresponds to the most shallow water condition. Since the keel is very close to the sea bed in this condition, a much finer mesh may have been needed to better capture the hydrodynamic effects between the keel and the sea floor. Additionally, it is clearly visible from the figures that in both motion modes the potential flow panel methods over-predict the motion responses compared to the experiments. When the CFD results are compared to those obtained from the panel methods, it can be concluded that the CFD method predicts the motion responses much better than potential flow theory, particularly for pitch motion. It should be mentioned that the differences between

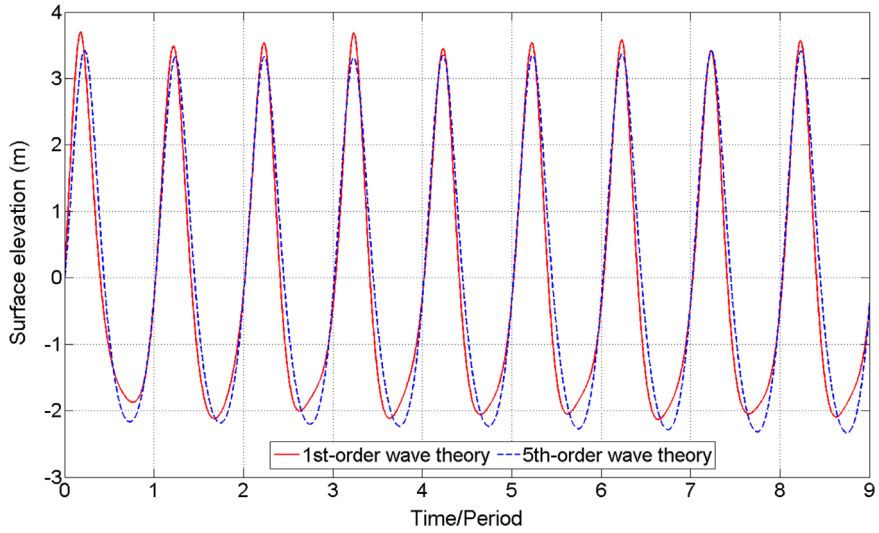

Fig. 12. Comparison of shallow water waves (T_w=12.133 s, τ=7.98) simulated using the first- and fifth-order Stokes wave theories at a water depth of 22.68 m at one wavelength away from the inlet.

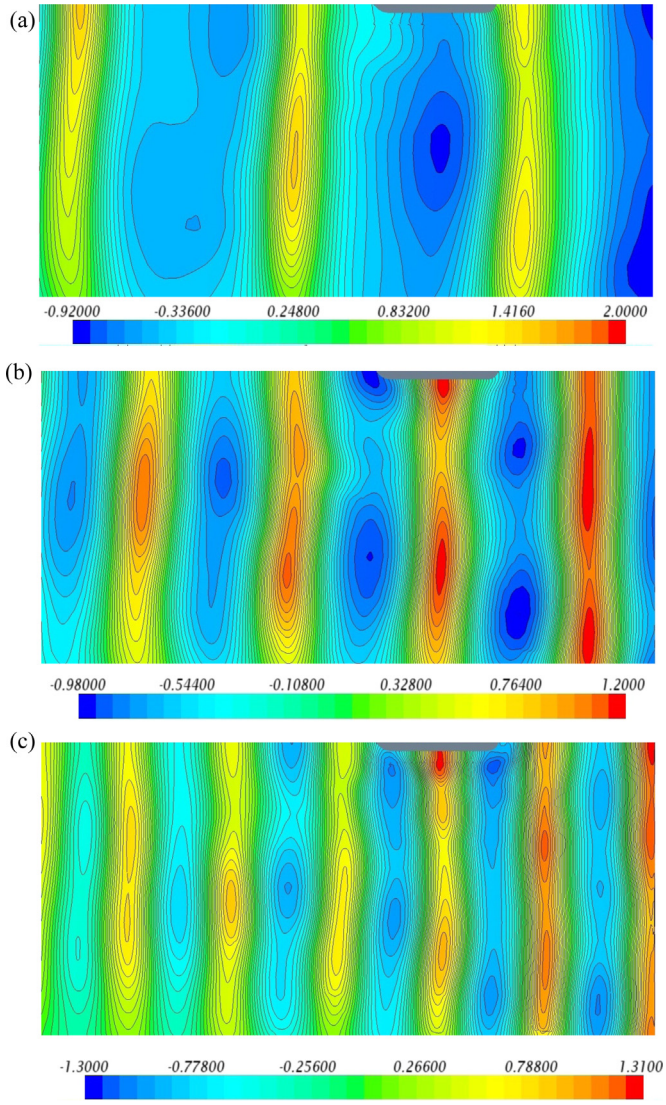

Fig. 13. Comparison of instantaneous wave patterns generated around the vessel by unit wave amplitude at a water depth of 22.68 m, for various non-dimensional frequencies $\omega'=1.12$, (b) $\omega'=1.69$, (c) $\omega'=2.25$.

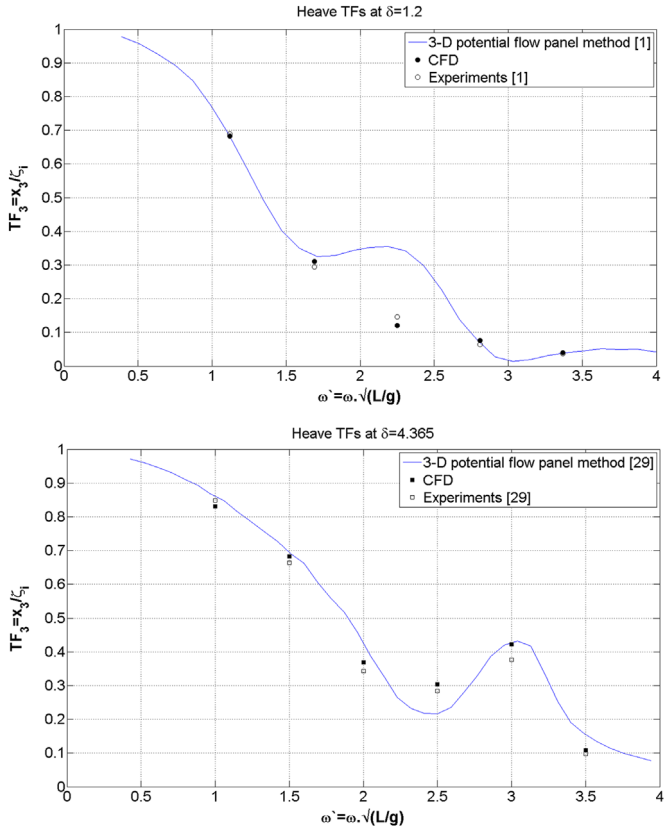

Fig. 14. Comparisons of the heave transfer functions using different methods in two different shallow water depths at zero speed. The upper half shows the responses at $\delta=1.2$, and the lower half shows the responses at $\delta=4.365$.

the experimental results and the panel methods may stem from the coarse panel generation and the assumptions made in the potential flow theory. It should also be borne in mind that the most recently developed 3-D potential flow theory-based codes, such as the Rankine source panel methods, may give more successful motion predictions than those presented in this paper.

It may be useful to emphasise that many previous studies, such as Schmitke (1978), have shown that viscous effects are likely to be the most significant, particularly in high amplitude waves and at high Froude numbers. Tezdogan et al. (2015) also came to the same conclusion in their study. They compared the URANS and potential flow theory results for the vertical motions of the KCS in response to head waves (in deep water) at two operational conditions (design speed and low speed), with the aim of evaluating the advantages of slow steaming operational conditions in terms of fuel consumption and CO_2 emissions. Their findings showed that the discrepancies between the URANS and potential flow theory results are amplified at higher Froude numbers (Fn). Since the simulations in the current work were performed at $Fn=0$, the problem considered in this study was essentially close to the potential flow problem. It is highly likely that the viscous effects would be much more significant if the vessel had a high forward speed.

Once the current URANS method was successfully validated, another set of simulations were repeated at $\delta=3.0$, in order to more precisely assess the effect of water depth on ship motions.

For all three water depths, the heave and pitch responses, predicted using our CFD model, are compared in Fig. 16, over the non-dimensional wave frequencies. For each combination of transfer function and water depth, a curve was fitted through the obtained results using a Piecewise Cubic Hermite Interpolating Polynomial, in order to provide a better comparison among the responses.

From the comparison shown in Fig. 16, it is clear to note that as the water depth becomes shallower, the heave amplitudes tend to decrease, whereas the pitch amplitudes tend to increase at low frequencies (or in long incident waves). However at high frequencies, a slight decrease is recognised in pitch responses as the water depth decreases. It can also be seen that for this tanker model, the maximum pitch response occurs when the ratio between wavelength and ship length (λ/L) is around 1.0. Therefore, it is observed that, while the water depth to the draft ratio decreases, the peak in the pitch transfer functions shifts towards the lower frequencies. It is also worth noting that the RAO curves in Fig. 16 show the same trend as those presented by Kim and Kim (2013), who, as explained earlier, carried out similar analyses for a 100-m Series 60 ship model using the 3-D Rankine panel method.

Aside from presenting the results graphically, the heave and pitch transfer functions predicted by CFD, EFD and potential flow theory at three different h/T ratios are tabulated in Table 6, in order to provide a distinctive comparison among the different methods.

4.6. Additional demonstration

As discussed earlier, Oortmerssen (1976) claims that in shallow

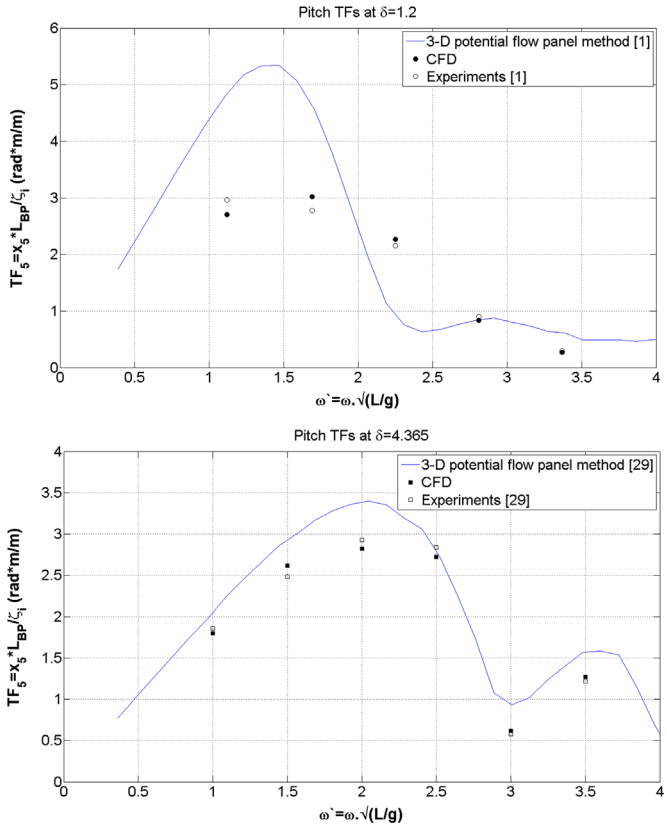

Fig. 15. Comparison of the pitch transfer functions using different methods in two different shallow water depths at zero speed. The upper half shows the responses at $\delta=1.2$, and the lower half shows the responses at $\delta=4.365$.

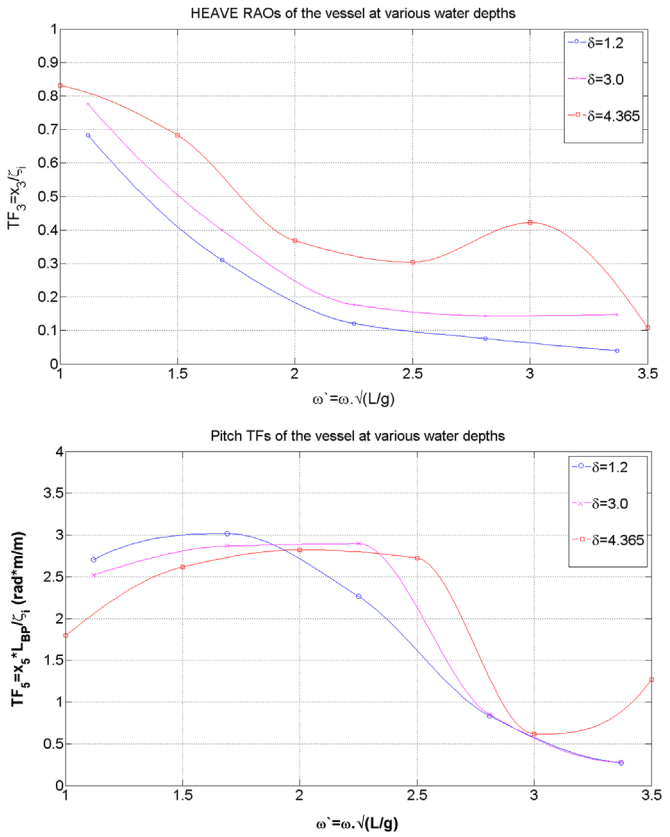

Fig. 16. A comparison of the ship responses (obtained using CFD) to incident head waves over the nondimensional frequency numbers in the three different shallow waters. The upper and lower halves show the heave and pitch transfer functions of the tanker, respectively.

water, three dimensional effects become significant such that the water flow passes partly underneath the ship and partly around the two ship ends. In order to validate this claim, the velocity vectors around the stern of the vessel are plotted in Fig. 17 in the deepest and shallowest cases. As can be clearly seen in the figure, in the shallowest case the flow partly passes around the stern. The same features could be observed in the other shallow water cases, meaning that 3-D effects become more pronounced as the water becomes shallower.

For the purpose of visualisation, Fig. 18 shows the responses of the tanker to the incident head waves in a wave period. An animated version of Fig. 18 is also provided in Electronic Annex I (The video legend: *Motions of the tanker over one wave period of time in the shallowest water*). This video was created from snapshots at each time step over two wave periods of time. Furthermore, Fig. 19 illustrates the change in the wall shear stress exerted on the ship hull over one wave period of time.

Supplementary material related to this article can be found online at http://dx.doi.org/10.1016/j.oceaneng.2016.06.047.

Fig. 20 displays the change in the turbulent viscosity ratio of the water around the ship hull due to the ship motions over one wave period. The turbulent viscosity ratio is proportional to a turbulent Reynolds number. This may be a good indication of how to express the change in turbulence of a fluid flow. As can be seen from Fig. 20, an almost homogenous turbulence dispersion across the flow is observed throughout the ship length. However, in all four snapshots, the turbulence peaks in magnitude around the ship bow due to the reflected incident waves from the bow.

It should be noted that the additional CFD results shown in Figs. 18–20 were taken from the results obtained for Case 1.1 (involving the shallowest water depth and the smallest wave frequency).

5. Concluding remarks and discussion

URANS simulations to predict the heave and pitch responses of a full scale very large tanker model to incident head waves were carried out at a zero forward speed. All analyses were performed using a commercial RANS solver, Star-CCM+, version 9.0.2.

Firstly, a numerical modelling set up was proposed in order to perform such analyses in shallow water using CFD. All procedures regarding mesh generation, treatment of wall functions, time step selection and wave modelling were presented in detail in the paper.

Next, a verification study was carried out to assess the uncertainties of the CFD model. The results obtained from this study suggested that the numerical uncertainties in the finest-grid solution for the heave and pitch transfer functions are predicted as 2.21% and 3.00%, respectively. These values become 1.48% and 1.78%, respectively, when the numerical uncertainty in the smallest time-step solution is predicted.

Following this, before beginning the seakeeping analyses, a series of simulations were performed with nonlinear shallow water waves, to observe the change in their form inside the computational domain. It was observed that the wave amplitudes mostly decrease as the waves propagate further down inside the domain. Also, additional simulations with the waves revealed that the waves simulated using the fifth-order theory give more successful results compared to those simulated using the first-order wave theory.

Following this, sixteen simulation cases, which were composed of various combinations of water depth and wave frequency, were applied to the tanker model. The results were compared to the experimental data and also to those obtained from potential flow

Table 6
The transfer functions by three different methods (Error (E) is based on EFD data).

Case no.	h/T	TF_3					TF_5				
		CFD		EFD	Potential flow theory		CFD		EFD	Potential flow theory	
C	δ	Result	E (%)		Result	E (%)	Result	E (%)		Result	E (%)
1.1	1.2	0.682	**−1.01**	0.689	0.685	**−0.50**	2.705	**−8.72**	2.964	4.845	**63.49**
1.2		0.310	**5.16**	0.294	0.328	**11.44**	3.017	**8.78**	2.774	4.608	**66.12**
1.3		0.121	**−16.97**	0.146	0.352	**140.78**	2.266	**5.18**	2.154	0.925	**−57.05**
1.4		0.076	**19.28**	0.064	0.055	**−14.53**	0.833	**−7.50**	0.901	0.845	**−6.16**
1.5		0.040	**9.21**	0.037	0.033	**−9.23**	0.274	**−7.94**	0.297	0.645	**116.88**
2.1	3	0.775	–	–	–	–	2.521	–	–	–	–
2.2		0.399	–	–	–	–	2.868	–	–	–	–
2.3		0.177	–	–	–	–	2.895	–	–	–	–
2.4		0.144	–	–	–	–	0.849	–	–	–	–
2.5		0.148	–	–	–	–	0.281	–	–	–	–
3.1	4.365	0.831	**−2.20**	0.849	0.857	**0.93**	1.796	**−3.38**	1.859	1.887	**1.52**
3.2		0.683	**2.84**	0.664	0.692	**4.16**	2.619	**5.43**	2.484	2.930	**17.97**
3.3		0.368	**7.25**	0.343	0.408	**19.21**	2.824	**−3.49**	2.926	3.432	**17.32**
3.4		0.304	**7.28**	0.284	0.246	**−13.41**	2.725	**−4.08**	2.841	2.778	**−2.23**
3.5		0.422	**11.88**	0.377	0.432	**14.49**	0.617	**6.17**	0.581	0.932	**60.50**
3.6		0.108	**9.83**	0.098	0.153	**55.25**	1.271	**4.77**	1.214	1.545	**27.33**

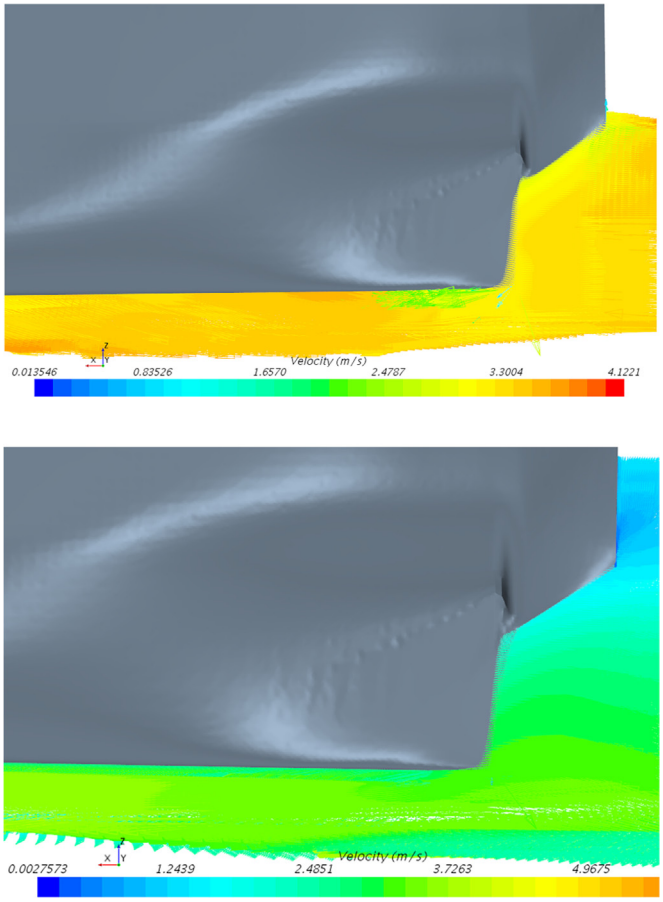

Fig. 17. Velocity contours around the stern of the vessel: the top and below figures show the shallowest and deepest cases, respectively.

panel methods. The main results drawn from this comparison can be listed as follows:

1. The transfer functions, obtained using the CFD method, showed fairly good agreement with the available experimental data. The differences between our results and the experimental results were slightly more pronounced at $\delta=1.2$, where the keel is closest to the sea bed. Also, it was obvious that the 3-D panel methods over-predict the heave and pitch transfer functions compared to the experimental results. Overall, the URANS method predicted the motion responses much more successfully than the potential flow theory, particularly for pitch motions.
2. It was concluded that as water becomes shallower, heave motions decrease, whilst pitch motions increase at low frequencies. On the other hand, at high frequencies, a slight decrease was observed in pitch responses as the water depth decreases.
3. For the tanker model in question, the maximum pitch response occurred in waves of length equal to, or around, the ship length ($\lambda/L=1.0$). It was observed that when the water depth decreased, the peak in the pitch transfer functions shifted to lower frequencies.

5.1. Discussion and future work

It should be noted that CFD-based numerical approaches can only give approximate results. The differences between reality and numerical results stem from the errors which occur in each stage of the numerical modelling process (Ferziger and Peric, 2002). Xiao (2012) states that numerical methods contain at least three forms of systematic errors, namely; modelling error, discretisation error, and iterative error. Ferziger and Peric (2002) point to the fact that even if the Navier–Stokes equations are solved exactly, the solution may still not resemble reality. CFD users should therefore validate their results against experiments. CFD is a useful tool at hand, however it may give misleading results if the physical problem is not modelled correctly. The authors believe that in order to favour the successful modelling of an incident, it is of critical importance to consider every parameter which may be at play in a given situation.

This research has provided a very useful starting point for further studies on ship behaviour and performance in shallow water. This study should be extended to include simulations in beam or oblique seas, to predict roll motions, for which the discrepancies between URANS methods and potential flow theory are expected to be amplified. However, it should be borne in mind that in this case, the number of generated mesh and the required computational effort will be doubled as the use of the symmetry

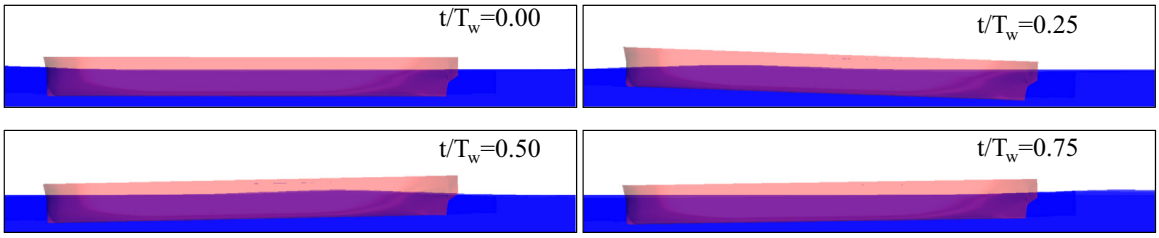

Fig. 18. Four snapshots of motions of the tanker and the elevation of the free surface in one wave period ($\delta=1.2$).

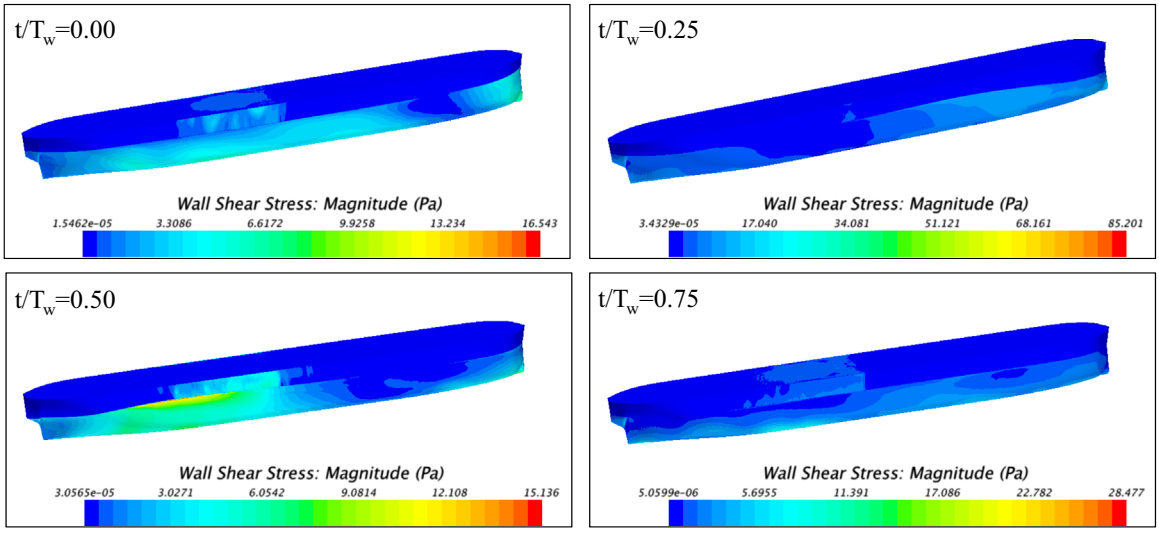

Fig. 19. Four snapshots of the changes in wall shear stress over one wave period of time.

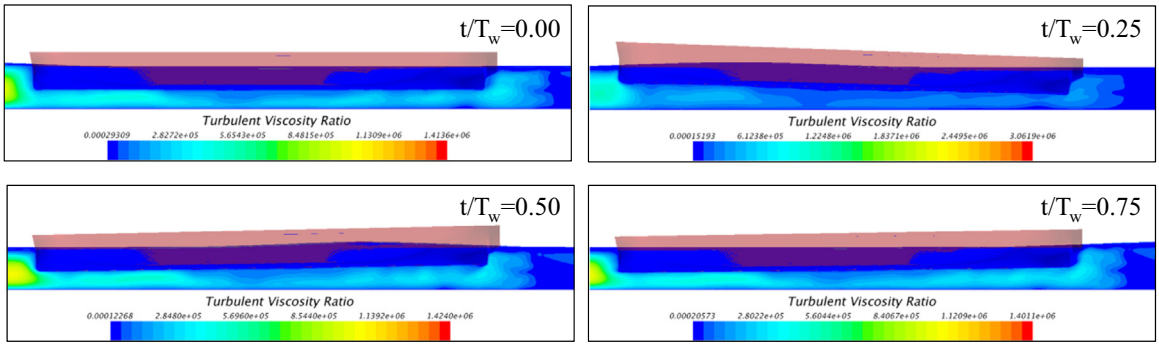

Fig. 20. Four snapshots of the changes in the turbulent viscosity ratio of the water around the ship's hull due to ship motions over one wave period of time ($\delta=1.2$).

boundary condition in the centre line of the ship and the domain will no longer be valid.

As discussed in the previous section, the viscous effects become significant at high Froude numbers. For this reason, this study should also be extended to incorporate high forward speed effects into the numerical simulations. Using the proposed URANS method, the added resistance and motion responses of a vessel due to waves in shallow water should be investigated, as this would be another piece of novel research. Also, a similar study can be repeated by using the Cnoidal wave theory and the results can be compared to those obtained using the first- or fifth-order Stokes waves.

As clearly shown in this study, ship motions significantly change in shallow water area compared to those in deep water. Without a doubt this change alters a vessel's operability and habitability performance. Using the methodology presented in Tezdogan et al. (2014), it would be very interesting to calculate how a vessel's operability changes when entering into a shallow water area. Another piece of interesting future study would be to investigate high speed vessel wake wash using CFD. In order to achieve this, Tezdogan et al. (2016)'s recent published paper may be a good start point.

Acknowledgements

The authors are grateful for the EPSRC support for the project on 'Shipping in Changing Climates' (EPSRC Grant No. EP/K039253/1) which enabled them to carry out the research reported in this paper.

The results were obtained using the EPSRC funded ARCHIE-WeSt High Performance Computer (www.archie-west.ac.uk). EPSRC Grant no. EP/K000586/1. The underlying data in this paper is openly available from the University of Strathclyde data repository at: http://dx.doi.org/10.15129/bb47acb8-a807-48c9-ac9e-6e689defa5ea

References

International Towing Tank Conference (ITTC), 2014. Ocean Engineering Committee, Final report and recommendation to the 27th ITTC. In: Proceedings of the 27th ITTC, Copenhagen. Available from: ⟨http://ittc.info/downloads/Proceedings/27th%20Conference/1-6%20Seakeeping%20Committee.pdf⟩ (accessed 15.09.14.).

International Towing Tank Conference (ITTC), 2011. Practical guidelines for ship CFD applications. In: Proceedings of the 26th ITTC, Rio de Janeiro – Brazil. Available from: ⟨http://ittc.sname.org/CD%202011/pdf%20Procedures%202011/7.5-03-02-03.pdf⟩ (accessed 10.09.14.).

CD-Adapco. User guide STAR-CCM+ Version 9.0.2, 2014.

Beukelman, W., Gerritsma, J., 1982. The distribution of hydrodynamic mass and damping of an oscillating shipform in shallow water. In: Proceedings of 11th Scientific and Methodological Seminar on Ship Hydrodynamics, pp. 297–329, Varna, Bulgaria.

Boreel, L.J., 1974. Wave action on large offshore structures. In: Proceedings of Conference on Offshore Structures, London, England.

Castiglione, T., He, W., Stern, F., Bova, S., 2014. URANS simulations of catamaran interference in shallow water. J. Mar. Sci. Technol. 19 (1), 33–51. http://dx.doi.org/10.1007/s00773-013-0230-5.

Celik, I.B., Ghia, U., Roache, P.J., Freitas, C.J., 2008. Procedure for estimation and reporting of uncertainty due to discretization in CFD applications. J. Fluids Eng. Trans. ASME 130 (7), 078001.

Chan HS. A three-dimensional technique for predicting first and second order hydrodynamic forces on a marine vehicle advancing in waves. University of Glasgow, Glasgow, UK, 1990.

Choi, J., Yoon, S.B., 2009. Numerical simulations using momentum source wavemaker applied to RANS equation model. Coast. Eng. 56 (10), 1043–1060. http://dx.doi.org/10.1016/j.coastaleng.2009.06.009.

Cosner, R.R., Oberkampf, W.L., Rumsey, C.L., Rahaim, C.P., Shih TI-P. AIAA Committee on standards for computational fluid dynamics: Status and plans. In: Proceedings of 44th Aerospace Sciences Meeting and Exhibit, Reno, Nevada.

Das, S., Cheung, K.F., 2012. Scattered waves and motions of marine vessels advancing in a seaway. Wave Motion 49 (1), 181–197.

Date, J.C., Turnock, S.R., 1999. A study into the techniques needed to accurately predict skin friction using RANS solvers with validation against Froude's historical flat plate experimental data. Southampton, UK, University of Southampton. (Ship Science Reports, (114)).

Daubert, A., 1970. Quelques considerations sur les differentes simulations et methodes de calcul du comportement des structures immergees ou flottantes en mer. La. Houille Blanche 2, 159–173.

Det Norske Veritas. Environmental conditions and environmental loads. Recommended Practice DNV-RP-C205, April 2007.

Endo, H., 1987. Shallow-water effect on the motions of three-dimensional bodies in waves. J. Ship Res. 31 (1), 34–40.

Enger, S., Peric, M., Peric, R., 2010. Simulation of flow around KCS-hull. In: Proceedings from Gothenburg 2010-A Workshop on Numerical Ship Hydrodynamics, Gothenburg.

Fenton, J.D., 1985. A fifth-order Stokes theory for steady waves. J. Waterw. Port. Coast. Ocean Eng. 111 (2), 216–234.

Fenton, J.D., 1979. A high-order cnoidal wave theory. J. Fluid Mech. 94 (1), 129–161.

Ferziger, J.H., Peric, M., 2002. Computational Methods for Fluid Dynamics, 3rd ed. Springer, Berlin.

Field, P.L., 2013. Comparison of RANS and Potential Flow Force Computations for the Onr Tumblehome Hullform in Vertical Plane Radiation and Diffraction Problems, MSc thesis. Virginia Polytechnic Institute and State University, Blacksburg, VA.

Garisson, C.J., Chow, P.Y., 1972. Wave forces on submerged bodies. J. Waterw. Harb. Coast. Eng. Div. 98 (3), 375–392.

Hess, J.L., Smith, A.M.O., 1964. Calculation of nonlifting potential flow about three-dimensional bodies. J. Ship Res. 8 (2), 22–44.

Jachowski, J., 2008. Assessment of ship squat in shallow water using CFD. Arch. Civil. Mech. Eng. 8 (1), 27–36.

Kim, C.H., 1968. The influence of water depth on the heaving and pitching motions of a ship moving in longitudinal regular head waves. Schiffstechnik 15 (79), 127–132.

Kim, T., Kim, Y., 2013. Numerical analysis on floating-body motion responses in arbitrary bathymetry. Ocean Eng. 62, 123–139. http://dx.doi.org/10.1016/j.oceaneng.2013.01.012.

Kim, S.P., Lee, H.H., 2011. Fully nonlinear seakeeping analysis based on CFD simulations. In: Proceedings of the 21st International Offshore and Polar Engineering Conference, Hawaii, USA, pp. 970–974.

Korteweg, D.J., Vries, G., 1895. On the change of form of long waves advancing in a rectangular canal, and on a new type of long stationary waves. Philos. Mag. Ser. 39 (240), 422–443 5.

Kring, D.C., 1994. Time Domain Ship Motions by a Three-dimensional Rankine Panel Method. Massachusetts Institute of Technology, Cambridge, USA.

Larsson, L., Stern, F., Visonneau, M., 2011. CFD in ship hydrodynamics- Results of the Gothenburg 2010 Workshop. Computational Methods in Marine Engineering IV (MARINE 2011), pp. 17–36.

Li, L., 2001. Numerical seakeeping predictions of shallow water effect on two ship interactions in waves. Dalhousie University, Halifax, Nova Scotia.

Oortmerssen, G.V., 1976. The Motions of a Moored Ship in Waves. Publication No. 510. Netherlands Ship Model Basin, Waganingen, The Netherlands.

Oortmerssen, G.V., 1976. The motions of a ship on shallow water. Ocean Eng. 3, 221–255. http://dx.doi.org/10.1016/0029-8018(76)90025-1.

Oortmerssen, G.V., 1972. Some aspects of very large offshore structures. In: Proceedings of 9th Symposium on Naval Hydrodynamics, p. 957–1001, Paris, France.

Ozdemir, Y.H., Barlas, B., Yilmaz, T., Bayraktar, S., 2014. Numerical and experimental study of turbulent free surface flow for a fast ship model. Brodogradnja 65 (1), 39–54.

Pinkster, J.A., 1980. Low Frequency Second Order Wave Exciting Forces on Floating Structures PhD-thesis. Delft University of Technology.

Prakash, S., Chandra, B., 2013. Numerical estimation of shallow water resistance of a river-sea ship using CFD. Int. J. Comput. Appl. 71 (5), 33–40.

Querard, A.B.G., Temarel, P., Turnock, S.R., 2008. Influence of viscous effects on the hydrodynamics of ship-like sections undergoing symmetric and anti-symmetric motions, using RANS. In: Proceedings of the ASME 27th International Conference on Offshore Mechanics and Arctic Engineering (OMAE), Estoril, Portugal, pp. 1–10.

Richardson, L.F., 1911. The approximate arithmetical solution by finite differences of physical problems involving differential equations, with an application to the stresses in a Masonry dam. Philos. Trans. R. Soc. Lond. Ser. A-Contain. Pap. Math. Phys. Character 210, 307–357.

Roache, P.J., 1998. Verification and Validation in Computational Science and Engineering. Hermosa Publishers, Albuquerque.

Roy, C.J., Blottner, F.G., 2001. Assessment of one- and two-equation turbulence models for hypersonic transitional flows. J. Spacecr. Rocket. 38 (5), 699–710.

Sakamoto, N., Wilson, R.V., Stern, F., 2007. Reynolds–Averaged Navier–Stokes simulations for high-speed wigley hull in deep and shallow water. J. Ship Res. 51 (3), 187–203.

Schmitke, R.T., 1978. Ship sway, roll, and yaw motions in oblique seas. Trans. Soc. Nav. Arch. Mar. Eng. 86, 26–46.

Sclavounos, P.D., Nakos, D.E., 1988. Stability analysis of panel methods for free surface flows with forward speed. In: Proceedings of 17th Symposiumon on Naval Hydrodynamics, p. 173–193, DenHague, The Netherlands.

Simonsen, C.D., Otzen, J.F., Joncquez, S., Stern, F., 2013. EFD and CFD for KCS heaving and pitching in regular head waves. J. Mar. Sci. Technol. 18 (4), 435–459. http://dx.doi.org/10.1007/s00773-013-0219-0.

Stern, F., Wilson, R., Shao, J., 2006. Quantitative V&V of CFD simulations and certification of CFD codes. Int. J. Numer. Methods Fluids 50 (11), 1335–1355.

Tezdogan, T., Demirel, Y.K., Kellett, O., Khorasanchi, M., Incecik, A., Turan, O., 2015. Full-scale unsteady RANS CFD simulations of ship behaviour and performance in head seas due to slow steaming. Ocean Eng. 97, 186–206. http://dx.doi.org/10.1016/j.oceaneng.2015.01.011.

Tezdogan, T., Incecik, A., Turan, O., 2014. Operability assessment of high speed passenger ships based on human comfort criteria. Ocean Eng. 89, 32–52. http://dx.doi.org/10.1016/j.oceaneng.2014.07.009.

Tezdogan, T., Incecik, A., Turan, O., 2016. A numerical investigation of the squat and resistance of ships advancing through a canal using CFD. J. Mar. Sci. Technol. 21 (1), 86–101. http://dx.doi.org/10.1007/s00773-015-0334-1.

Troesch, A., Beck, R.F., 1974. Experiments on ship motions in shallow water. Report No. 149. The Department of Naval Architecture and Marine Engineering, The University of Michigan, College of Engineering.

Wilson, R., Paterson, E., Stern, F., 1998. Unsteady RANS CFD method for naval combatants in waves. In: Proceedings of the 22nd Symposium on Naval Hydrodynamics, pp. 532–549, US.

Xiao, Q., 2012. Theory and Practice of Marine CFD (Lecture Notes). University of Strathclyde, Glasgow.

Xing, T., Stern, F., 2010. Factors of Safety for Richardson Extrapolation. J. Fluids Eng. Trans. ASME 132 (6), 061403.

Yuan, Z.-M., Incecik, A., Jia, L., 2014. A new radiation condition for ships travelling with very low forward speed. Ocean Eng. 88, 298–309. http://dx.doi.org/10.1016/j.oceaneng.2014.05.019.

Zou, L., Larsson, L., 2013. Numerical predictions of ship-to-ship interaction in shallow water. Ocean Eng. 72, 386–402. http://dx.doi.org/10.1016/j.oceaneng.2013.06.015.